Inducing maximal localization with fractal waveguide arrays

Jonathan Guglielmon and Mikael C. Rechtsman

Fractal waveguide arrays induce maximal localization

Jonathan Guglielmon[1] and Mikael C. Rechtsman[1]

[1]*Department of Physics, The Pennsylvania State University, University Park, PA 16802, USA*

(Dated: March 25, 2019)

The ability to transmit light through an array of closely packed waveguides while minimizing interwaveguide coupling has important implications for fields such as discrete imaging and telecommunications. Proposals for achieving these effects have involved phenomena ranging from Floquet-induced flat bands to Anderson localization. An approach based on Anderson localization is beneficial since every eigenstate localizes and this localization is applicable to arbitrarily large propagation distances. However, the localization lengths can be large so that sites within a given finite region can exhibit significant crosstalk. Here we pose an optimization problem in which we seek to maximally confine the eigenstates. We demonstrate that, for strongly detuned waveguides arranged in an equally spaced lattice in 1D and a square lattice in 2D, optimal eigenstate localization can be achieved by fractal potentials. We further show that these structures possess a localization-delocalization phase transition in both 1D and 2D. The structures are related to a more general family of self-similar potentials that can be constructed on the class of k-partite lattices satisfying the property that each sublattice forms a rescaled copy of the original lattice. The structures may also be approximated by a family of periodic structures, and we characterize the performance of these approximations in comparison to the full aperiodic structures.

I. INTRODUCTION

The transmission of light through a discrete array of waveguides has important applications ranging from imaging to telecommunications [1–3]. In these contexts, each waveguide serves as an independent channel through which information is transmitted. Ideally, the waveguides should be closely packed in order to maximize the amount of information that can be encoded into a given cross-sectional area of the array. Unfortunately, this leads to an increase in the mode overlap of adjacent waveguides and produces problematic interwaveguide crosstalk. One potential way to eliminate this crosstalk is through dynamic localization [4–8], where a periodic spatial modulation of the waveguide trajectory causes renormalized nearest-neighbor couplings to vanish. This is equivalent to introducing a Floquet drive that generates a flat quasienergy band. Alternatively, one can take the waveguides to be straight and either arrange them into a structure, such as a Lieb lattice, that exhibits a non-dispersive flat band [9–13], or introduce a detuning between adjacent waveguides by offsetting their propagation constants to reduce the effective strength of the interwaveguide coupling [14, 15]. Here, the waveguide propagation constants are tuned either by adjusting the waveguide diameter or by varying the refractive index of the core. Another avenue takes inspiration from the phenomenon of Anderson localization [16–21] and uses disorder to localize the system's eigenstates.

Each of these approaches comes with a distinctive set of limitations. A Floquet system introduces bending losses and, if the waveguides deviate from a precisely specified, curved trajectory, the renormalized couplings will no longer vanish. Structures, like the Lieb lattice, that contain flat bands also contain additional bands that are dispersive. Since an arbitrary input state will excite a combination of the flat and dispersive bands, general states are not preserved under evolution through the structure. Additionally, higher-neighbor couplings add dispersion to the bands so that coupling is only suppressed out to a finite propagation distance determined by the associated coupling length. Similarly, strategies that rely on detuning the propagation constants using a pattern that is periodic in the transverse plane will produce crosstalk at long distances since the structure is subject to Bloch's theorem and therefore has extended eigenstates. In contrast, disorder generates Anderson localization, which applies to every eigenstate and suppresses diffraction out to infinite propagation distance. However, the degree to which crosstalk is reduced crucially depends on the localization lengths which, in two dimensions, can be large. It is therefore natural to pose the question: to what extent can the localization lengths be reduced by more precisely tailoring the configuration of individual waveguide propagation constants?

In this work, we demonstrate that, in the regime in which waveguide propagation constants can be strongly detuned, maximally localized eigenstates can be generated by self-similar configurations in which sites are recursively detuned from one another over increasingly larger spatial scales. Being aperiodic, these structures possess the advantages of disorder arising from eigenstate localization, but they surpass disorder in their ability to tightly confine the eigenstates. We characterize these structures, noting the existence of a localization-delocalization phase transition in both 1D and 2D. We also characterize a closely related series of periodic structures with increasingly larger unit cells that are able to suppress diffraction out to increasingly larger propagation distances. These periodic structures can be naturally organized according their complexity, beginning with very simple periodic arrangements and approaching the full aperiodic fractal. This organization provides a systematic method for realizing approximations to the
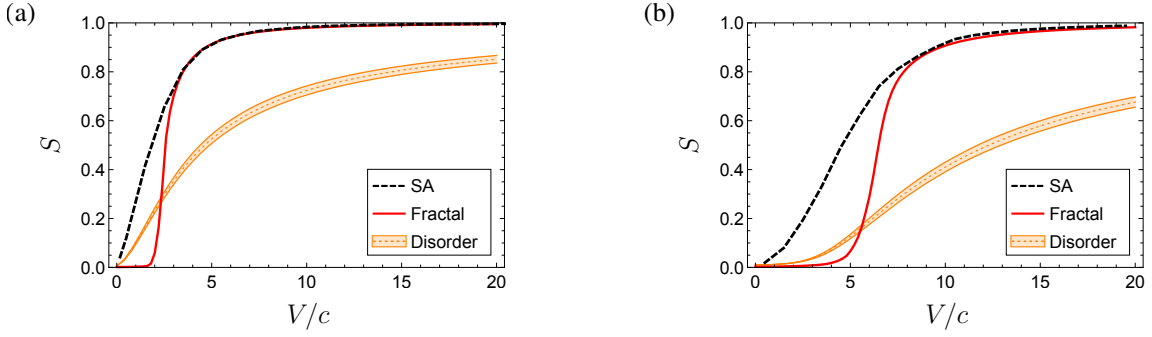
FIG. 1. Objective function at $z \to \infty$ (average eigenstate participation ratio) for different onsite energy configurations. Panels (a) and (b) respectively show the results for 1D and 2D systems. The dashed black curve was obtained using simulated annealing to optimize the onsite energies. The dashed orange curve shows the results for onsite disorder averaged over many disorder realizations and the shaded orange region corresponds to one standard deviation from the mean. The red curve shows the results for the fractal structure described in the text, using $\alpha = 0.25$ and $\alpha = 0.36$ for the 1D and 2D cases, respectively. In the strongly detuned regime, the fractal structure surpasses disorder in both 1D and 2D and performs comparably to the optimized structures.

fractal in a way that tailors the complexity of the structure to the requirements of a given application.

II. OBJECTIVE FUNCTION AND ITS OPTIMIZATION

We consider light evolving through an array of coupled waveguides and note that, while we develop our results in the photonic context, they in fact generalize to systems that can be modeled as a lattice of coupled degrees of freedom with a tunable onsite potential. In such a waveguide array, the waveguides act as lattice sites that possess bound modes whose profiles weakly overlap with their neighbors so that the system can be modeled using tight-binding theory [22]. Throughout our analysis, we assume that the waveguides are single-mode. The onsite energy, V_i, of each waveguide is determined by the deviation of the waveguide propagation constant from its background value, which can be controlled by varying either the waveguide diameter or the refractive index of the waveguide core. This yields a tight-binding Schrödinger equation

$$i\partial_z \psi_i(z) = \sum_j (c_{ij} + V_i \delta_{ij}) \psi_j(z) \qquad (1)$$

where i labels the individual waveguides of the structure (on a lattice of arbitrary dimension), ψ_i is the amplitude of the electric field in waveguide i, z is the propagation distance measured along the axial direction of the waveguides, and c_{ij} is the coupling constant between sites i and j.

At the input facet, one injects an electric field profile ψ_i with intensity amplitudes $|\psi_i|^2$ representing the input data. The light propagates through the structure and produces an output intensity pattern $|\psi_i'|^2$ representing the output data. In this context, eigenstate localization

is desirable in order to keep $|\psi_i'|^2$ as similar as possible to $|\psi_i|^2$. Motivated by the ability of disorder to induce localization, we pose the question: what is the optimal way to distribute the onsite energies, V_i, so as to produce maximal localization?

To answer this question, we define an objective function, $S(z)$, related to how much the intensity distribution of input states changes during evolution over a propagation distance z. In choosing such a function, we note that the sum of squared differences in position space intensities between the initial and final states is given by

$$\sum_i \left(|\psi_i|^2 - |\psi_i'|^2 \right)^2 = \sum_i \left(\langle \psi | M_i | \psi \rangle \right)^2 \qquad (2)$$

where the M_i are operators defined by $M_i = |e_i\rangle\langle e_i| - |u_i\rangle\langle u_i|$. Here $|e_i\rangle$ is the unit vector with all except the ith entry equal to zero and $\langle u_i|$ is the ith row vector of the unitary evolution operator $U(z)$ evaluated at a propagation of distance z. Keeping $|\psi\rangle$ general, we then seek to minimize $\sum_i ||M_i||^2$, where we use the entry-wise matrix norm $||A||^2 = \sum_{ij} |A_{ij}|^2$. It is simple to show that this is equivalent to maximizing $\sum_i |\langle u_i | e_i \rangle|^2 = \text{tr} |U(z)|^2$, where the absolute value is taken element-wise when $U(z)$ is expressed in the position basis. In general, $\text{tr} |U(z)|^2$ can oscillate rapidly as a function of z, so that a solution that is optimal at z may fail to be optimal at a nearby point $z + \Delta z$. To avoid this problem, we perform an integral over z so as to capture information about the behavior over the entire interval:

$$S(z) = \frac{1}{Nz} \int_0^z dz' \, \text{tr} |U(z')|^2 . \qquad (3)$$

Here we have further normalized the function by the number of sites, N, so that $S(z) \in [0,1]$ with $S(z) = 1$ implying that an arbitrary single-site injection will remain perfectly localized at the injection site out to propagation distance z.
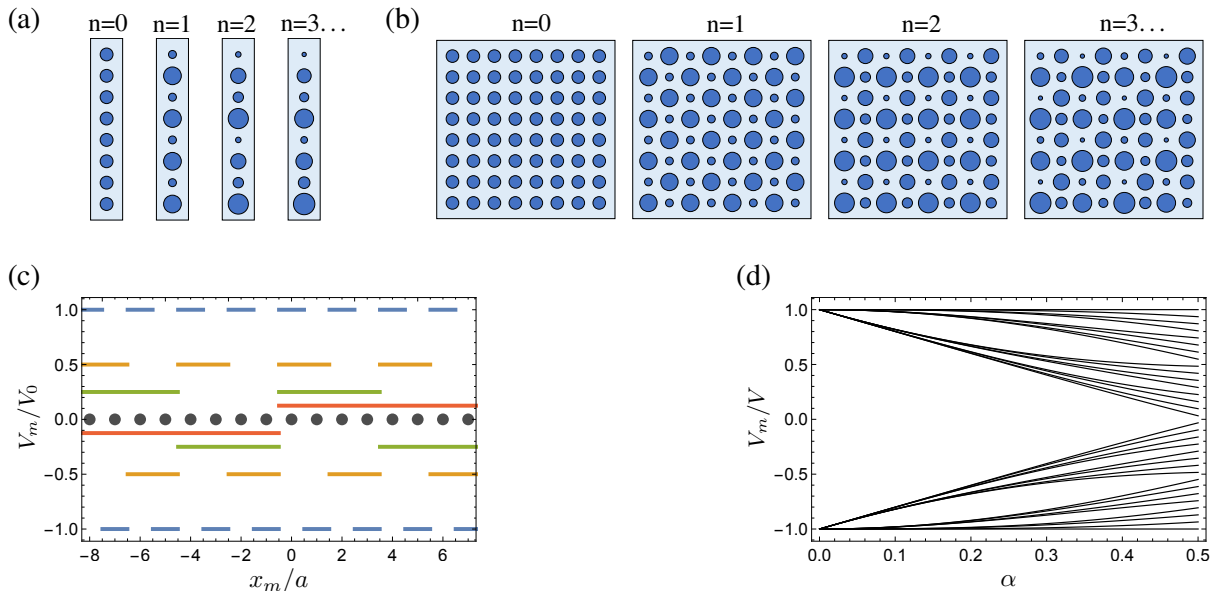
FIG. 2. Construction of the fractal potentials described in the text. Panel (a) shows the construction of the 1D case and panel (b) the 2D case, where the onsite energies have been encoded in the radii of the circles (with the variation of the radii exaggerated for clarity). The structure is generated by recursive application of a detuning procedure in which each increase in the recursion level, n, results in an exponentially larger unit cell, with the full aperiodic structure obtained in the $n \to \infty$ limit. Panel (c) shows the first four terms of the decomposition of the 1D potential into square waves, with the sites of the lattice overlaid on the x-axis. Panel (d) shows the dependence of the onsite energies on the parameter α for a 32-site periodic approximation to the fractal (truncated at $n = 5$). In this plot, the onsite energies at a given α are simply sorted by energy and do not directly correspond to locations on the lattice. The onsite energies are normalized by V, which, in this case, is taken to be the full range of the potential covered by this periodic approximation.

In our optimization, we will take the infinite propagation distance limit of $S(z)$ and only evaluate $S(z)$ at finite z when characterizing a set of periodic structures that are closely related to the self-similar potential that we will introduce later. In this limit, $S(z)$ bears a close relation to the participation ratios of the energy eigenstates: assuming the system possesses no degeneracies, we have

$$\lim_{z \to \infty} S(z) = \langle P_E \rangle \qquad (4)$$

where $\langle P_E \rangle$ represents the average of the participation ratios over all the energy eigenstates (see Appendix B).

In this work, we restrict attention to potentials defined over an equally spaced array in 1D and a square lattice in 2D. We note, however, that the structures we uncover can be constructed on a more general class of k-partite lattices satisfying the property that the k independent sublattices form rescaled copies of the original lattice. This includes the important case of the triangular lattice, which is used in applications that seek to maximize the density of lattice sites. We perform an optimization of $S(z)$ at $z \to \infty$ (that is, the average eigenstate participation ratio in Eq. 4) using simulated annealing on a 256 site chain in 1D and a 16×16 lattice in 2D. In both cases, we impose periodic boundary conditions and include only nearest-neighbor coupling c. We restrict the onsite energies to lie within a finite interval $[-V, +V]$ and

perform independent optimizations for different values of V.

The results of the optimization are plotted in Fig. 1 and provide a baseline standard for ideal performance. For comparison, we have also shown the corresponding curve for a disordered potential (with onsite disorder drawn uniformly from the interval $[-V, +V]$) using the same system size as in the optimization and averaged over 1000 disorder realizations. We note, in particular, that the optimum is achieved not by disorder but by some other potential. While the optimized results themselves provide a useful measure of ideal performance, it is desirable to locate structures that perform at the level indicated by the optimization and that are amenable to a precise description that enables us to construct the structures for arbitrarily large system size, both to provide a well-defined class of structures that can be further studied and to verify that the optimized results do not rely on finite size effects. We find that this can be done in the regime of strong detuning, where optimal performance can be achieved by a family of self-similar potentials that we construct below. While these highly ordered potentials perform comparably to the optimized structures, we note that our optimization suggests that the optimum may be non-unique or nearly degenerate with other structures. In particular, the numerically optimized structures themselves both contain features associated with the po-

tentials that we construct below, as well as features that differ from these potentials. The fact that these features do not significantly change the performance of the structures suggests the non-uniqueness of the optimum.

III. FRACTAL POTENTIALS

A. Construction and performance

We now demonstrate that the degree of localization achieved by the numerically optimized structures can be achieved by a fractal potential that can be constructed analytically. We begin by fixing an onsite energy scale V_0 and a dimensionless parameter $\alpha \in [0, \frac{1}{2}]$ that controls the structure of a Cantor set from which the onsite energies are sampled (see discussion below). Noting that the lattice (a 1D linear array or 2D square lattice) can be made to be bipartite, we subdivide the lattice into two sublattices to which we respectively assign onsite energies of $\pm V_0$. Since each of the sublattices themselves form rescaled copies of the original lattice (rotated by $\pi/4$ in the 2D case), we can independently repeat the detuning procedure on each sublattice, this time using a smaller detuning of $\pm \alpha V_0$. In general, at a recursion level n, we apply a detuning of $\pm \alpha^n V_0$ to obtain the structure at level $n+1$. This procedure is illustrated in Fig. 2.

When this process is iterated sending $n \to \infty$, the structure converges to an aperiodic potential with onsite energies contained in the interval $[-V, +V]$, where $V = V_0/(1-\alpha)$. In the 1D case, the resulting potential can be written as:

$$V_m = V_0 \sum_{k=0}^{\infty} \alpha^k s \left(\frac{m + 1/2}{2^{k+1}} \right) \tag{5}$$

where $s(x)$ is an odd, unit-period square wave that alternates between ± 1. Here the potential has been evaluated at site $x_m = ma$, where a is the nearest-neighbor spacing. See Fig. 2(c) for an illustration of this square wave expansion. In the 2D case, the potential takes on a similar form:

$$V_{mn} = V_0 \sum_{k=0}^{\infty} \left[\alpha^{2k} s \left(\frac{m+1/2}{2^{k+1}} \right) + \alpha^{2k+1} s \left(\frac{n+1/2}{2^{k+1}} \right) \right] \tag{6}$$

where the pair of indices on V_{mn} indicate that the potential has been evaluated at site $\mathbf{x}_{mn} = m\mathbf{R}_1 + n\mathbf{R}_2$ with $\mathbf{R}_1 = a(1,0)$ and $\mathbf{R}_2 = a(1,1)$.

In Fig. 1, we have plotted the objective function for these structures to show that, in the regime of strong detuning, they perform comparably to the optimized results from simulated annealing. We note that we have increased the system size in producing the plots for these structures to a 1024 site chain in 1D and a 32×32 structure in 2D to demonstrate that our fractal model achieves optimal performance for system sizes beyond that used
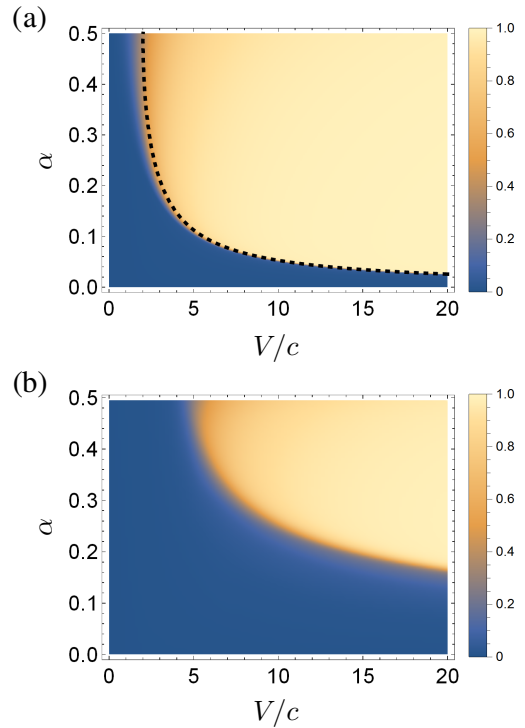
FIG. 3. Average eigenstate participation ratio for (a) the 1D and (b) the 2D fractal structures. The sharp transition indicates a phase transition in which the eigenstates go from being extended to being localized. A 1024 site chain and 32×32 site grid were used for the 1D and 2D structures, respectively. In the 1D case, an analytical approximation for the phase boundary can be calculated for small α and yields the boundary shown in panel (a) as a dashed line.

in the optimization. As before, we have imposed periodic boundary conditions at the system's edges. We also mention that, in the regime of nearly perfect localization ($S \sim 1$), the fractal yields an order of magnitude improvement over disorder in terms of the potential strength required to generate such strong localization. For example, an objective function value of $S = 0.98$ is achieved by the 1D fractal at $V/c \sim 10$ and by the 2D fractal at $V/c \sim 20$. In contrast, achieving this value, on average, using disorder requires $V/c > 100$ (which resides outside the plot region in Fig. 1) in both 1D and 2D. Finally, we have included in the Supplemental Material [23] a set of animations in which we sweep the strength of the potential across the V/c axis of Fig. 1 while showing the output obtained by evolving an image through the corresponding structure, with the results for the fractal and disordered potentials compared side-by-side. We have included separate animations for the cases of coherent imaging and incoherent imaging [24], with the fractal yielding noticeable improvements over disorder in both cases.

B. Localization-delocalization phase transition

To further study the localization properties of these potentials, we show in Fig. 3 the average eigenstate participation ratio as a function of V/c and α. We note the presence of a sharp boundary at which the participation ratio rapidly changes, indicating a transition between a phase with extended eigenstates and a phase with localized eigenstates. As shown in Appendix A, an analytical approximation to the phase boundary can be computed in 1D using a renormalization group based calculation and is shown in Fig. 3(a) as a dashed line. We contrast these phase transitions with the behavior of disordered systems, which exhibit localization for arbitrarily weak disorder in both 1D and 2D and only exhibit a localization-delocalization transition in 3D. The presence of such phase transitions in lower-dimensional potentials has previously been observed for structures such as the Aubry-André model [25, 26].

C. Cantor set associated with the onsite energies

The onsite energies that appear in the construction of the fractal potentials lie in a Cantor set determined by the parameter α. Here we describe this set for the general case, alluded to above, where the potential is constructed on a k-partite lattice that satisfies the property that the k independent sublattices form rescaled copies of the original lattice. The two fractal potentials described above constitute the $k = 2$ case since both the 1D array and 2D square lattice can be partitioned so as to be bipartite. The general k-partite construction proceeds analogously to the bipartite case. In particular, we begin by choosing an energy scale, V_0, and a parameter $\alpha \in [0, \frac{1}{k}]$. We then divide the interval $[-V_0, +V_0]$ into k equally spaced onsite energies, $\{v_1, ..., v_k\}$, and assign these onsite energies to the k sublattices so as to detune neighboring sites. This constitutes the $n = 1$ level structure. To generate the $n = 2$ level structure, we repeat this procedure independently on each sublattice, this time detuning over a smaller interval $[v_i - \alpha V_0, v_i + \alpha V_0]$ centered on the v_i associated with the respective sublattice. This process is repeated infinitely many times to yield the final onsite energy configuration.

Note that iterating the above process yields—for the onsite energies centered on v_i—a bounded set contained in the interval

$$\left[v_i - \sum_{m=1}^{\infty} \alpha^m V_0, v_i + \sum_{m=1}^{\infty} \alpha^m V_0\right] = [v_i - \alpha V, v_i + \alpha V] \quad (7)$$

where $V = V_0/(1-\alpha)$. Note that this interval has length αL with $L = 2V$. In particular, the procedure has divided the full interval $[-V, +V]$ of length $L = 2V$ into k equally spaced, closed subintervals of length αL such that all onsite energies of the final structure lie within these subintervals. Note that the subintervals generally
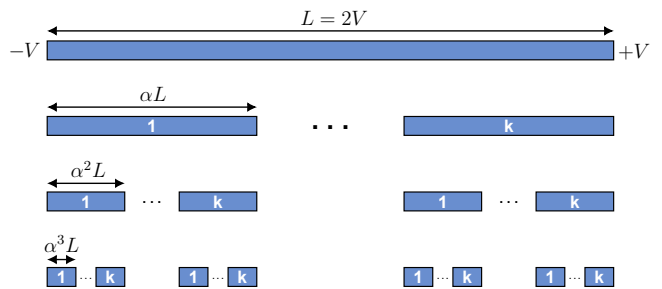

FIG. 4. Cantor set associated with the onsite energies of the fractal structures for the general k-partite case. The energy interval $[-V, +V]$ of length $L = 2V$ is divided into k smaller, equally spaced subintervals, each of length αL. The gaps between these subintervals represent excluded ranges of onsite energies that are not used in the structure. Iterating this process of subdivision yields a Cantor set within which the onsite energies reside.

do not cover the full interval $[-V, +V]$ since they have a combined length of $k(\alpha L)$ with $\alpha \in [0, \frac{1}{k}]$. The spaces between the subintervals form regions of excluded energies that are not assigned to any site in the structure. This is illustrated in Fig. 4. Iterating this argument over higher levels of detuning yields a Cantor set within which the onsite energies of the final structure reside. Note that, as the collection of onsite energies is countable (since the underlying lattice is countable), the actual onsite energies only form a proper subset of this Cantor set. Finally, we note that this construction makes clear why the general k-partite structure is parameterized by $\alpha \in [0, \frac{1}{k}]$: the boundary case, $\alpha = \frac{1}{k}$, yields a subdivision of the interval $[-V, +V]$ into subintervals that fully span the interval (i.e., which leave no excluded regions).

D. Periodic approximations

In practice, implementations of an onsite energy configuration will be subject to restrictions on how many distinct onsite energies are available within fabrication tolerances and to perturbations such as higher-neighbor couplings and disorder. Here we discuss how our structure can be implemented with a constrained set of available onsite energies and provide in Appendix C a characterization of the effects of perturbations. As the fractal is constructed via a recursive series of detuning operations—each yielding a larger unit cell requiring a larger but finite number of distinct onsite energies—it provides a natural set of periodic structures that can be used to approximate the full structure. Here we characterize these structures based on the maximal propagation distance at which they are able to suppress crosstalk.

As the truncated structures are periodic, the eigenstates will be extended and the corresponding value of $\lim_{z\to\infty} S(z)$ vanishes. As a result, a different metric is necessary to study the periodic truncations. We therefore
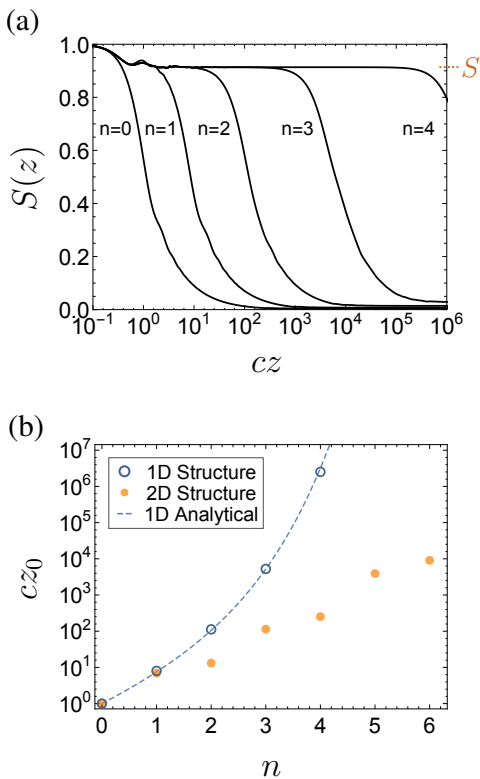
FIG. 5. Behavior of periodic truncations of the fractal. (a) Finite z objective function plotted for the 1D structure with $\alpha = 0.25$ and $V/c = 5$ (parameters which, for the full structure, yield a localized phase) truncated at various detuning levels n. The function follows the value S associated with the full aperiodic structure out to some critical propagation distance z_0 which diverges as $n \to \infty$. (b) Dependence of z_0 on n for a 1D structure defined by the parameters mentioned above and a 2D structure defined by parameters $\alpha = 0.36$ and $V/c = 10$. In the 1D case, the dashed curve shows the analytical result obtained from the effective coupling $c(N)$ discussed in the text.

relax our criteria and evaluate $S(z)$ at finite propagation distance. Defining $S \equiv \lim_{z \to \infty} S(z)$ evaluated for the full aperiodic fractal, a given periodic truncation will produce a function $S(z)$ that approximately follows the value S out to some critical propagation distance, z_0, beyond which it approaches zero. This effect is demonstrated in Fig. 5(a), where we plot $S(z)$ for the 1D structure truncated at unit cells of size 2^n for $n = 0, \ldots, 4$. The behavior in the 2D case is similar.

The propagation distance at which the function drops below S can be understood as the coupling length scale of diffraction associated with the average width of the 2^n individual bands of the periodic system (i.e., by interpreting the average bandwidth ΔE_{avg} in terms of an effective coupling c_{eff} via $\Delta E_{\text{avg}} = 4c_{\text{eff}}$ for the 1D array and $\Delta E_{\text{avg}} = 8c_{\text{eff}}$ for the 2D square lattice, and then computing an associated coupling length scale $z_0 \sim 1/c_{\text{eff}}$). In Fig. 5(b), we plot z_0, as extracted from the average bandwidth, as a function of n for both the 1D and 2D cases.

Here we see that increasing the level n of the truncation results in a drastic increase in the distance over which the structure is capable of suppressing diffraction. We further note that, in the 1D case, we can obtain an analytical approximation for this distance. Defining $N \equiv 2^n$ as the number of sites in the unit cell after n detuning operations, the effective coupling $c(N)$ that determines the coupling length takes the form $c(N) = c\,e^{-\gamma(N-1)}/N^{\beta}$ with $\gamma = \log(2\alpha V_0/c)$, $\beta = \log_2(1/\alpha)$, and c the nearest-neighbor coupling of the physical structure (see Appendix A). The associated length scale is then $z_0 \sim 1/c(N)$ which is plotted in Fig. 5(b) as a dashed line. Note that in the above approximation, the distance over which diffraction is suppressed scales exponentially in N but only as a power law in V_0, demonstrating the sense in which it can be more effective to increase the structure's complexity (i.e., the size, N, of the unit cell) instead of merely increasing the strength of the detuning V_0.

IV. CONCLUSION

Motivated by the ability of disordered potentials to suppress diffraction, we have studied the question of how one should structure a potential to achieve maximal localization. We conclude that, while disorder is efficient in the sense of being able to induce localization for arbitrarily weak disorder, it is inefficient in the degree of localization it generates. In particular, we have found that, when the range of onsite energies is large relative to the coupling, maximally efficient localization can be obtained by constructing a highly ordered, self-similar potential. Like the disordered case, the resulting structure is aperiodic and, as such, circumvents Bloch's theorem, allowing for the existence of localized eigenstates. Unlike disorder, however, it exhibits a localization-delocalization transition in both 1D and 2D. Almost immediately upon passing through the transition, the potential induces eigenstate localization that is maximal in comparison to a baseline obtained using simulated annealing. In comparison to approaches based on engineered flat bands, our structure is advantageous in that it avoids the bending losses associated with a Floquet drive and does not possess the additional dispersive bands associated with static flat-band systems like the Lieb lattice. Furthermore, unlike the flat band of a Lieb lattice, the addition of moderate strength higher-neighbor couplings (discussed in Appendix C) does not significantly alter the performance.

A useful feature of the fractal potentials arises from their construction via a series of simpler periodic structures that are labeled by the recursion level, n, at which the construction of the fractal is terminated. These structures suppress diffraction out to a propagation distance that diverges rapidly with n. The complexity of the structure can therefore be tailored to the total propagation distance required by a given application, with larger values of n being better suited for applications that re-

quire larger propagation distances—a feature that could find use for crosstalk reduction in spatially multiplexed fibers for use in long-distance data transmission. The limiting aperiodic structures thus provide a direct recipe for designing structures that suppress diffraction at a given propagation distance. Additionally, they clarify the existence of a localization-delocalization transition that affects the ability of the periodic truncations to suppress diffraction at long distances.

The objective function value, S, associated with the full fractal structure also provides information about the performance of the periodic structures. In the regime with localized eigenstates, the value of S may be intuitively thought of as restricting the radius within which crosstalk can occur, where the radius shrinks to zero as S increases. For the full fractal, this radius of restriction applies even out to infinite propagation distance. For the periodic structures, the value of S is effectively inherited from the full fractal, but only out to a finite propagation distance z_0. This inherited value provides the periodic structures with the same crosstalk-restricting radius, but only out to z_0, which is in turn determined by n. The periodic structures are therefore characterized by a pair of quantities: (S, n). The quantity S determines the degree to which light will remain localized around its injection site, and it can be increased by increasing the strength of the detuning. The quantity n determines the maximal propagation distance at which this degree of localization can be maintained, and it can be increased by introducing higher levels of detuning that increase the structure's complexity.

ACKNOWLEDGMENTS

Appendix A: Analytical approximation to phase boundary

Here we compute an analytical approximation for the localization-delocalization phase boundary for the 1D fractal structure discussed in the text. We begin by considering an equally spaced 1D array in which adjacent sites are detuned by $\pm u$ (Fig. 6). Assuming a nearest-neighbor coupling of c, the eigenstates form two bands with energies given by

$$E(k) = \pm\sqrt{u^2 + 4c^2 \cos^2(k/2)} \qquad (A1)$$

$$= \pm(u^2 + 2c^2)^{1/2}\sqrt{1 + \frac{2c^2}{u^2 + 2c^2}\cos k} \qquad (A2)$$
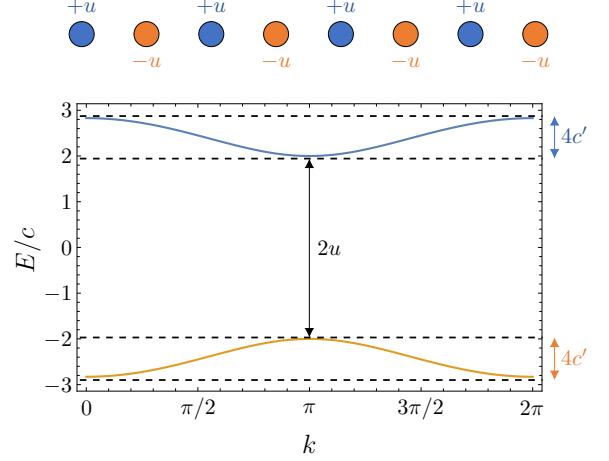

FIG. 6. Illustration of a detuned linear array and its band structure. In the strongly detuned regime, the upper and lower bands become highly localized on the $+u$ and $-u$ sublattices, respectively. In this limit, we may reinterpret the two bands as forming two independent arrays governed by a modified interwaveguide coupling c' that is determined by the width of the individual bands.

which can be expanded as

$$E(k) = \pm\left[(u^2 + 2c^2)^{1/2} + \frac{c^2 \cos k}{(u^2 + 2c^2)^{1/2}} + \ldots\right] \quad (A3)$$

We now consider the regime where $c/u \ll 1$ and neglect higher-order terms in the expansion. Noting that, in this approximation, the individual bands obey a dispersion proportional to $\cos(k)$ (up to an offset in energy), we may reinterpret the two bands as forming two distinct linear arrays with a modified nearest-neighbor coupling determined by the bandwidth:

$$c' = \frac{c^2}{2(u^2 + 2c^2)^{1/2}} \qquad (A4)$$

$$= c^2/(2u) + O(c^3/u^3). \qquad (A5)$$

We now make an additional approximation in which we note that, in the regime $c/u \ll 1$, the eigenstates of the upper and lower bands are highly localized on the $+u$ and $-u$ sublattices, respectively. Since the construction of the potential described in the text proceeds by independently reapplying the detuning procedure on these two sublattices (with smaller detuning energies $\pm\alpha u$), we may iterate the procedure discussed above to generate a flow of the effective interwaveguide coupling. In particular, for the next iteration, we repeat the above calculation using a new coupling $c' = c^2/(2u)$ and a new detuning $u' = \alpha u$. This will again generate a modified coupling $c'' = c'^2/(2u') = c^4/(8\alpha u^3)$. More generally, we define c_k and u_k as the effective coupling and energy detuning at recursion level k. In particular, for the structure defined in the text $u_k = \alpha^k V_0$.

Note that in the approximation introduced above, the eigenstates will localize when the ratio $r_k \equiv c_k/u_k$ goes

to zero for large k, as this indicates that the asymptotic energy detuning becomes infinitely large relative to the corresponding effective coupling. From the procedure introduced above, we have $c_{k+1} = c_k^2/(2u_k)$ and hence

$$r_{k+1} = \left(\frac{u_k}{2u_{k+1}}\right) r_k^2. \tag{A6}$$

This recursion relation can be solved exactly, yielding

$$\log r_k = 2^k \left\{ \sum_{m=1}^{k} \frac{1}{2^m} \log\left(\frac{u_{m-1}}{2\,u_m}\right) + \log r_0 \right\}. \tag{A7}$$

Using the detuning function $u_k = \alpha^k V_0$ and denoting $c_0 = c$, this simplifies to

$$\log r_k = 2^k \log\left(\frac{c}{2\alpha V_0}\right) - \log\left(\frac{1}{2\alpha}\right) \tag{A8}$$

so that $\lim_{k\to\infty} r_k = 0$ when

$$\frac{V_0}{c} > \frac{1}{2\alpha}, \tag{A9}$$

indicating eigenstate localization. In the opposite regime, $V_0/c < 1/(2\alpha)$, the ratios formally diverge, $\lim_{k\to\infty} r_k = \infty$, indicating that the asymptotic onsite energies become negligible relative to the corresponding couplings, suggesting the presence of extended eigenstates. We note, however, that in this latter regime, the expansion used above with $c/u \ll 1$ begins to break down after some finite number of iterations k. Hence, the behavior of the eigenstates in this regime must be verified numerically. Finally, to keep the derivation consistent with the assumption $c/u \ll 1$, we require α appearing in Eq. A9 to be small. In this regime, the bound is in good agreement with the numerical results, as shown in the localization-delocalization phase diagram of the main text (which shows the boundary curve defined by Eq. A9 after using the relation $V = V_0/(1-\alpha)$).

We note that Eq. A8 also contains information about the critical propagation distances, z_0, which, as discussed in the text, determine the maximal distance at which the periodic truncations of the structure are capable of suppressing diffraction. In particular, a periodic structure truncated after k detuning levels has an associated coupling length scale $z_0 \sim 1/c_k$ and from Eq. A8 we have

$$\log\left(\frac{c_k}{c}\right) = (2^k - 1) \log\left(\frac{c}{2\alpha V_0}\right) - k \log\left(\frac{1}{\alpha}\right). \tag{A10}$$

Noting that after k detuning operations, the unit cell contains $N = 2^k$ sites, we rewrite the coupling as a function of system size via $c_k \to c(N)$ with $N = 2^k$ yielding

$$c(N) = c\, e^{-\gamma(N-1)}/N^\beta \tag{A11}$$

with $\gamma = \log(2\alpha V_0/c)$ and $\beta = \log_2(1/\alpha)$. Note that this result is only applicable to the localized phase where we have $\gamma > 0$. The formal divergence of $c(N)$ in the delocalized phase is unphysical and signals the breakdown of the expansion used above. In particular, in the delocalized phase, the $c(N)$ decay slower than the u_k, so that eventually the condition $c/u \ll 1$ fails to be satisfied.

Appendix B: Expressions for $S(z)$ at finite and infinite z

We now provide a useful formula for the objective function, $S(z)$, at finite z and derive the relation of its infinite distance limit to the average eigenstate participation ratio. Consider a Hamiltonian H that is diagonalized by a unitary matrix $\mathcal{V}$ and has eigenvalues E_i. That is, $(\mathcal{V}^\dagger H \mathcal{V})_{ij} = \delta_{ij} E_i$. We define matrices $\Delta E_{ij} = E_i - E_j$, $W_{ij} = |\mathcal{V}_{ij}|^2$, and $M = W^T W$. We then have

$$\text{tr}\,|U(z)|^2 = \sum_{ijk} |\mathcal{V}_{ij}|^2 e^{-i(E_j - E_k)z} |\mathcal{V}_{ik}|^2 \tag{B1}$$

$$= \text{tr}\left[W e^{-i\Delta E z} W^T \right] \tag{B2}$$

$$= \text{tr}\left[\cos(\Delta E\, z) M \right] \tag{B3}$$

where in the last two lines the exponential and cosine are taken element-wise (i.e., are not the matrix exponential/matrix cosine) and we have used the fact that M is a symmetric matrix to conclude that the corresponding sine term vanishes. Integrating this result with respect to z, we obtain

$$S(z) = \frac{1}{Nz} \int_0^z dz'\, \text{tr}\,|U(z')|^2 \tag{B4}$$

$$= \frac{1}{N} \text{tr}\left[M \,\text{sinc}(\Delta E\, z) \right] \tag{B5}$$

where the sinc is taken element-wise. This form

$$S(z) = \frac{1}{N} \text{tr}\left[M \,\text{sinc}(\Delta E\, z) \right] \tag{B6}$$

expresses $S(z)$ purely in terms of the eigenvalues and eigenvectors of the system and is useful for evaluating $S(z)$ for periodic structures like those described in the text. For aperiodic structures, it is useful to take the limit $z \to \infty$. In the absence of degeneracies, we have $\lim_{z\to\infty} \text{sinc}(\Delta E_{ij} z) = \delta_{ij}$ so that

$$\lim_{z\to\infty} S(z) = \frac{1}{N} \text{tr} M. \tag{B7}$$

Finally, noting that the diagonal entries of M are equal to the eigenstate participation ratios $P_E = \sum_i |\langle x_i|E\rangle|^4$ with $|E\rangle$ normalized, we have

$$\lim_{z\to\infty} S(z) = \langle P_E \rangle. \tag{B8}$$

Appendix C: Characterization of the effect of perturbations

Here we characterize how the introduction of disorder and higher-order couplings to the fractal structure affects the resulting localization. To study the effect of
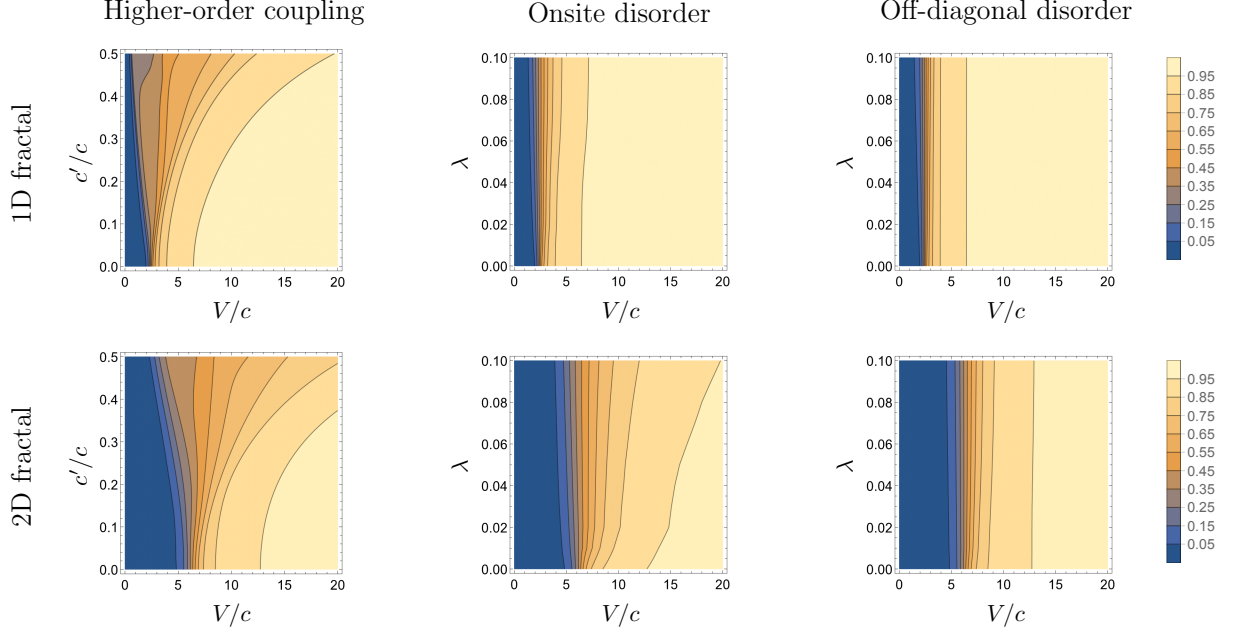
FIG. 7. Characterization of the dependence of the objective function on various types of perturbations introduced to the fractal structure. The upper and lower rows show the results for the 1D fractal and 2D fractal, respectively. As in Fig. 1 of the main text, we use $\alpha = 0.25$ for the 1D structure and $\alpha = 0.36$ for the 2D structure. The plots are colored according to the value of the objective function, S, and constant S contours are drawn as solid lines. The first column shows the effect of including couplings beyond nearest-neighbor, with c'/c representing the ratio between second-neighbor and first-neighbor couplings. The second and third columns show the effect of onsite disorder and off-diagonal disorder, respectively, as a function of the relative disorder strength λ.

higher-order couplings, we assume an exponential model, $c(r) = A \exp(-\gamma r)$, governing the dependence of the interwaveguide couplings on separation distance r. Note that for a model of this form, once both first-neighbor and second-neighbor couplings have been specified, all other higher-order couplings are determined. In our computations, we therefore specify the first two orders of couplings and then include all higher-order couplings in accordance with the exponential model. In the first column of Fig. 7, we plot the objective function, S, for the fractal as a function of V/c and c'/c, where c and c' are the first-neighbor and second-neighbor couplings, respectively, and V is the strength of the potential. In producing the plots for the 1D and 2D structures, we take $\alpha = 0.25$ and $\alpha = 0.36$, respectively. Note that taking the horizontal cut $c'/c = 0$ through the plot yields the objective function curve shown in Fig. 1 of the main text, where higher-neighbor couplings are turned off.

In studying the effect of disorder on the fractal, we separately consider both onsite disorder and off-diagonal disorder. In the case of onsite disorder, we perturb each onsite energy by an energy drawn uniformly from the interval $[-\lambda V, +\lambda V]$, where V is the strength of the unperturbed potential and λ is a factor that determines the relative strength of the disorder. Note that such onsite disorder will outweigh finer levels of onsite detuning that occur beyond some sufficiently large maximal recursion level n, the value of which depends on the strength of the

disorder. The structure may then be thought of as one of the periodic approximations to the fractal (discussed in the text) with the addition of disorder at a smaller energy scale. When realizing such a structure, one should then only realize this corresponding periodic approximation, since the higher levels of detuning that are outweighed by the disorder will only serve to add unnecessary additional complexity. We consider λ in the range $\lambda \in [0, 0.10]$. At each λ, we compute the objective function averaged over 250 disorder realizations using only nearest-neighbor couplings. The results are shown in the second column of Fig. 7. We perform an analogous calculation for the case of off-diagonal disorder. Here we randomly perturb the interwaveguide couplings by an amount drawn uniformly from the interval $[-\lambda c, +\lambda c]$ and, as before, compute the objective function averaged over 250 disorder realizations. The results are shown in the third column of Fig. 7.

As a concrete example utilizing the above results, consider a typical single-mode waveguide operating at $1550\,\mathrm{nm}$ with a cladding index $n_0 = 1.5$, an index contrast $\delta n = 3.0 \times 10^{-3}$, and a core diameter of $8\,\mu\mathrm{m}$. If we assume that the core diameter can be varied over $\pm 2\,\mu\mathrm{m}$, this yields an available onsite energy range of $\pm 18\,\mathrm{cm}^{-1}$ to be used in constructing the fractal potential. A 2% fabrication error in the waveguide diameters will introduce onsite disorder in the range $\pm 1.5\,\mathrm{cm}^{-1}$, yielding a relative disorder strength of approximately 10%. Taking

the 2D fractal as an example, this shifts the strength of the potential required to obtain an objective function value of $S = 0.95$ from approximately $V/c = 13$ to $V/c = 20$ (see the second column of Fig. 7). This remains a significant improvement over disorder, which requires $V/c > 100$ to achieve this value when averaged over disorder configurations. For second-neighbor couplings with amplitudes of less than 20% of the nearest-neighbor couplings, the value of V/c mentioned above remains nearly unchanged (see the first column of Fig. 7). Similarly, the introduction of random variations in the coupling amplitudes on the scale of 10% of the unperturbed couplings has little effect on the structure's performance, with $V/c = 13$ continuing to yield an objective function value of $S = 0.95$ (see the third column of Fig. 7).

[1] H. H. Hopkins and N. S. Kapany, Nature **173**, 39 (1954).
[2] D. J. Richardson, J. M. Fini, and L. E. Nelson, Nature Photonics **7**, 354 (2013).
[3] P. J. Winzer, Bell Labs Technical Journal **19**, 22 (2014).
[4] H. S. Eisenberg, Y. Silberberg, R. Morandotti, and J. S. Aitchison, Phys. Rev. Lett. **85**, 1863 (2000).
[5] S. Longhi, M. Marangoni, M. Lobino, R. Ramponi, P. Laporta, E. Cianci, and V. Foglietti, Phys. Rev. Lett. **96**, 243901 (2006).
[6] A. Szameit, I. L. Garanovich, M. Heinrich, A. A. Sukhorukov, F. Dreisow, T. Pertsch, S. Nolte, A. Tünnermann, S. Longhi, and Y. S. Kivshar, Phys. Rev. Lett. **104**, 223903 (2010).
[7] I. L. Garanovich, S. Longhi, A. A. Sukhorukov, and Y. S. Kivshar, Physics Reports **518**, 1 (2012).
[8] A. Crespi, G. Corrielli, G. D. Valle, R. Osellame, and S. Longhi, New Journal of Physics **15**, 013012 (2013).
[9] D. Guzmn-Silva, C. Meja-Corts, M. A. Bandres, M. C. Rechtsman, S. Weimann, S. Nolte, M. Segev, A. Szameit, and R. A. Vicencio, New Journal of Physics **16**, 063061 (2014).
[10] R. A. Vicencio and C. Meja-Corts, Journal of Optics **16**, 015706 (2014).
[11] R. A. Vicencio, C. Cantillano, L. Morales-Inostroza, B. Real, C. Mejía-Cortés, S. Weimann, A. Szameit, and M. I. Molina, Phys. Rev. Lett. **114**, 245503 (2015).
[12] S. Mukherjee, A. Spracklen, D. Choudhury, N. Goldman, P. Öhberg, E. Andersson, and R. R. Thomson, Phys. Rev. Lett. **114**, 245504 (2015).
[13] Y. Zong, S. Xia, L. Tang, D. Song, Y. Hu, Y. Pei, J. Su, Y. Li, and Z. Chen, Opt. Express **24**, 8877 (2016).
[14] K. L. Reichenbach and C. Xu, Opt. Express **15**, 2151 (2007).
[15] M. Koshiba, K. Saitoh, and Y. Kokubun, IEICE Electronics Express **6**, 98 (2009).
[16] P. W. Anderson, Physical review **109**, 1492 (1958).
[17] H. De Raedt, A. Lagendijk, and P. de Vries, Phys. Rev. Lett. **62**, 47 (1989).
[18] T. Schwartz, G. Bartal, S. Fishman, and M. Segev, Nature **446**, 52 (2007).
[19] S. Karbasi, C. R. Mirr, P. G. Yarandi, R. J. Frazier, K. W. Koch, and A. Mafi, Optics letters **37**, 2304 (2012).
[20] S. Karbasi, R. J. Frazier, K. W. Koch, T. Hawkins, J. Ballato, and A. Mafi, Nature Communications **5**, 3362 (2014).
[21] S. Karbasi, T. Hawkins, J. Ballato, K. W. Koch, and A. Mafi, Optical Materials Express **2**, 1496 (2012).
[22] F. Lederer, G. I. Stegeman, D. N. Christodoulides, G. Assanto, M. Segev, and Y. Silberberg, Physics Reports **463**, 1 (2008).
[23] See Supplemental Material at URL for simulations of image propagation through the fractal and disordered potentials.
[24] J. Goodman, *Introduction to Fourier Optics* (W. H. Freeman, 2017).
[25] S. Aubry and G. André, Ann. Isr. Phys. Soc. **3**, 18 (1980).
[26] Y. Lahini, R. Pugatch, F. Pozzi, M. Sorel, R. Morandotti, N. Davidson, and Y. Silberberg, Phys. Rev. Lett. **103**, 013901 (2009).